Ultrafast laser-induced topochemistry on metallic glass surfaces

Mathilde Prudent, Alejandro Borroto, Florent Bourquard, Stéphanie Bruyère, Florence Garrelie, Sylvie Migot, Jean-François Pierson, Jean-Philippe Colombier

Materials & Design 244 (2024) 113164

Contents lists available at ScienceDirect

Materials & Design

journal homepage: www.elsevier.com/locate/matdes

Ultrafast laser-induced topochemistry on metallic glass surfaces

Mathilde Prudent [a], Alejandro Borroto [b], Florent Bourquard [a], Stéphanie Bruyère [b], Sylvie Migot [b], Florence Garrelie [a], Jean-François Pierson [b], Jean-Philippe Colombier [a,*]

[a] UJM Saint-Etienne, CNRS, Institute of Optics Graduate School, Laboratoire Hubert Curien UMR CNRS 5516, F-42023 St-Etienne, France
[b] Université de Lorraine, CNRS, IJL, F-54000 Nancy, France

ARTICLE INFO

Keywords:
Ultrafast laser
Nanostructuring
LIPSS
Metallic glass thin films
Crystallization
Nanoparticles

ABSTRACT

Manufacturing multifunctional nanocomposite materials and engineered surface nanopatterns involves a strategic blend of topography, crystal structures, and chemistry. Here, we report the controllable formation of crystalline nanoparticles and intermetallic compounds on thin films of metallic glasses ($Zr_{50}Cu_{50}$, $Ti_{50}Cu_{50}$, and $Zr_{67}Ag_{33}$) irradiated by ultrafast laser beams. Mapping the structural modification of the photoexcited and subsequently heated alloys reveals previously neglected chemical reactions with air, offering a direct solution for incorporating nanoparticles into an amorphous oxide matrix and broadening the range of laser-induced surface self-organization features. Our findings are attributed to the occurrence and enrichment of oxygen surface contamination that reacts with selected elements of the metallic glasses. Additionally, the growth of the crystalline phase from undercooled liquid may originate from the dissolution of oxides. Finally, our results establish that the combination of crystalline nanoparticles on amorphous periodic patterns can be universally obtained in a wide range of binary systems of irradiated metallic glasses.

1. Introduction

A survey of biological surface behavior highlights the significant role played by the combination of topography and chemistry in achieving exceptional functional properties [1,2]. In the quest for desired performances, nature demonstrates intriguing physical phenomena that rely on precise topochemistry control. This is evident in the hydro-hygro-oleo-phobic properties that enable self-cleaning effects on lotus leaves and cicada wings [3], the unique adhesive abilities of gecko feet [4], or the drag reduction capabilities of shark skin [5]. Despite the remarkable success of biomimetic strategies developed for organic solids, polymers, semiconductors, and, more recently, 2D materials, surface engineering through the interconnected manipulation of structural arrangement, chemistry, and topography remains less explored and challenging in metallic materials [6,7]. The illumination of surface by ultrafast laser light has garnered considerable interest in recent years, with advancements in nanostructuring processes enabling energy localization on the nanoscale. This localization triggers original and exciting properties of nano-patterned surfaces [8,9]. Light-driven material arrangement and structural modifications hinge on the extreme local field enhancement, which orchestrates the interplay between inhomogeneous light coupling and polarization-oriented material response, in conjunction with the reaction with the surrounding gas environment [10]. The design of metallic nanostructures using ultrafast lasers, especially the formation of periodic ordered nanostructures through a regulated feedback mechanism known as laser-induced periodic surface structures (LIPSS) [11], aims to concentrate local light field energy into closely coupled regions. This concentration leads to intense photoexcitation, isochoric heating, and phase transitions. To manipulate physico-chemical surface properties, atomic and crystal rearrangements that occurs may be rationalized as a function of the irradiated material [12,13]. Consequently, a careful investigation of the light-induced surface response is required to enable the emerging of mesoscopic features from nanometric manipulations for complex materials as amorphous metals. In this work, detailed mapping of laser-induced changes reveals previously overlooked air-driven chemical reactions. These reactions create an amorphous oxide matrix with embedded nanoparticles. By revealing the crucial role of air-driven chemical reactions in laser-induced self-organization of metallic glasses, this study opens a new avenue for manipulating surfaces and designing advanced properties. Our finding underscores the importance of understanding and potentially mitigating the influence of oxygen during laser processing of metallic alloys. While achieving precise oxygen incorporation remains a challenge, this knowledge suggests a valuable guide for both minimizing adverse effects and harnessing potential benefits of oxygen for tailoring surface functionalities in these materials.

* Corresponding author.
E-mail address: jean.philippe.colombier@univ-st-etienne.fr (J.-P. Colombier).

https://doi.org/10.1016/j.matdes.2024.113164
Received 14 March 2024; Received in revised form 10 July 2024; Accepted 10 July 2024
Available online 15 July 2024

Metallic glasses, often referred to as amorphous metal alloys, have been a subject of intensive research since the 1960s, primarily due to their unique amorphous structure. Their inherent uniformity and the absence of grain boundaries endow them with a remarkable combination of properties compared to conventional polycrystalline materials. These properties include exceptional elastic strain (~ %2), which is significantly higher than that of most common crystalline metallic alloys (typically less than (< 1%), as well as corrosion resistance and high mechanical strength [14]. This strength results from the absence of microstructural features such as grains, grain boundaries, and dislocations, making them highly valuable for mechanical applications [15]. To address the limited ductility and plasticity of metallic glasses, researchers have recently developed heterogeneous microstructures in various systems by combining a glassy matrix with ductile crystalline phases [16–18]. It has been reported that composite microstructures containing crystalline phases exhibit improved toughness and plasticity under mechanical stress compared to monolithic glasses [16,19]. The *ex situ* composites can be prepared by directly introducing crystalline second phase as reinforcements into the glass-forming melt during processing. In order to substitute complex existing solutions based on crystalline phase introduction in glass-forming melt during processing, we propose to combine thin film metallic glass (TFMG) coating technology with ultrafast laser nanostructuring. Thin films produced through physical vapor deposition (PVD) exhibit enhanced ductility compared to bulk materials, and their micron-scale thickness is well-suited for precise ultrashort laser energy deposition, with affected depths often measured in hundreds or even tens of nanometers.

Ultrafast laser irradiation with pulse fluences in sub-threshold ablation regime opens up significant possibilities for precise and efficient fabrication of nano/microstructures on the surface of metals. Periodic features have been shown to offer various applications for example based on plasmonic, anti-reflective, antibacterial, and wettability properties via single pulse and multipulse irradiation [20–25]. In this laser fluence regime, the dynamic coupling between incoming light and the formed nanoroughness influences the local energy deposition and temperature gradients from pulse to pulse giving a positive feedback for periodic nanostructure ordering [26–29]. The periodic behavior of the topography is assigned to different mechanisms such as the coherent superposition of incident with scattered waves, the surface plasmon wave excitation, the near-field enhancement, and the corrugation-mediated feedback effects [30,31,28,10]. In addition to topography, ultrashort pulses were recognized to strongly disturb the structural arrangement of the material, with the opportunity to create exotic phases [32–34,12,35].

In this work, we explore the surface patterning of metallic glasses, notably $Zr_{50}Cu_{50}$, generating self-organized patterns at length scales comparable to the wavelength of light. Within this regime, local field enhancement is mediated by evolving surface topography, and the patterns growth is regulated through a strong feedback mechanism. Our investigation delves into the intricate interplay between incident light and laser-induced material modifications, emphasizing the interdependence of selective oxidation and the formation of nanocrystallites on the surface. To elucidate the coupling between incoming light and material alterations, we reveal the involvement of selective oxidation and the periodic emergence of face-centered cubic crystal structures of Cu on the amorphous surface. We achieve this by correlating topographical observations from cross-sectional transmission electron microscopy (TEM) analysis with energy-dispersive X-ray spectroscopy (EDS). Notably, the temperature-induced local oxidation of Zr centers appears to play a significant role in this complex process of topochemistry transformation.

2. Materials and methods

To achieve surface structuring of thin film metallic glasses, we employed ultrafast laser irradiation that leverages topography-induced feedback from successive pulses in an air environment to induce chemical modifications. Multipulse ultrafast laser irradiation involves a complex interplay of photo-thermal mechanisms, where absorbed energy and heat confinement interact with hydrodynamic processes, leading to phase transitions, melt flow, and material removal. Multiple laser pulses are essential for developing a stable laser-induced periodic surface structure pattern within an ultrashort laser spot, as previously reported for Zr-based metallic glasses, which uniquely form without bifurcations in bulk MG [36]. However, in TFMGs, the columnar morphology introduces roughness heterogeneities, impacting the uniformity of feedback effects and promoting the emergence of bifurcations [37].

2.1. Sample preparation

TFMGs were obtained by DC magnetron co-sputtering of metallic targets (Zr + Cu, Ti + Cu, or Zr + Ag) in an argon atmosphere. The films were deposited on (100)-oriented silicon single crystal substrates of 1.5×1.5 cm^2. The target-to-substrate distance was fixed at 9 cm for all types of TFMG. The depositions were performed using a rotating substrate holder to ensure chemical homogeneity of the films. The sputtering chamber was pumped down using a mechanical and a turbomolecular pump, achieving a base vacuum of 10^{-6} Pa. The deposition pressure was maintained at 1 Pa. The current applied to the sputtering targets was adjusted to achieve the desired compositions ($Zr_{50}Cu_{50}$, $Ti_{50}Cu_{50}$, and $Zr_{67}Ag_{33}$). The films were deposited without external heating or substrate bias. The self-established temperature at the substrate, measured using a thermocouple, did not exceed 45 °C C during growth. The resulting film thickness was optimized at 1.5 μm to balance PVD constraints with optical and thermomechanical management considerations. This thickness was chosen to be larger than the heat confinement length due to thermal electronic conduction, ensuring that the laser-induced effects are confined within the material. Additionally, this thickness helps to prevent delamination of the film by mitigating the reflection of the laser-generated pressure wave at the impedance change.

2.2. Ultrafast laser irradiation

For the ultrafast laser irradiation process, the laser pulses were delivered to the surface of TFMGs to form LSFL using a Ti:Sapphire femtosecond laser system (Legend Coherent Inc.). The laser has a central wavelength of $\lambda = 800$ nm, with a pulse duration of $\tau = 60$ fs at a repetition rate of $R = 1$ kHz (as shown in Fig. 1a). The linearly polarized laser pulses were attenuated and focused through a 250 mm achromatic lens at normal incidence. The focused laser spot exhibited a Gaussian profile with a spot size (at $1/e^2$) measuring $2\omega_0 = 56$ μm. The laser fluence quoted in this paper is the peak fluence $F = 2E/\pi\omega_0^2$, with E being the laser pulse energy. The single-shot damage threshold fluence of 0.08 J/cm^2 was determined using the D^2 method [38]. The fluence dependence of the observed topography was explored by performing additional experiments at different doses, varying both the laser fluence and the number of pulses, as well as the overlapping rates. Here, we focus on the most regular LSFL obtained after femtosecond laser irradiation with a peak fluence of 0.2 J/cm^2. Operating in a LIPSS generation regime offers the advantage of a structuring method that can be generalized to any composition or material. Regarding nanostructure spatial coherence over large areas, LIPSS offer an additional advantage for achieving high uniformity due to the seeding effect from the previously formed LIPSS pattern. This method is also easily reproducible, ensuring well-defined thermomechanical conditions just above the melting point and near the ablation threshold. The irradiated zone of interest forms a continuous and uniform line achieved through a static irradiation method by moving the sample holder. The latter moved in the electric field direction at a velocity of 2.8 mm/s, with 5 pulses delivered every 5 μm, resulting in a 96% overlap [39].

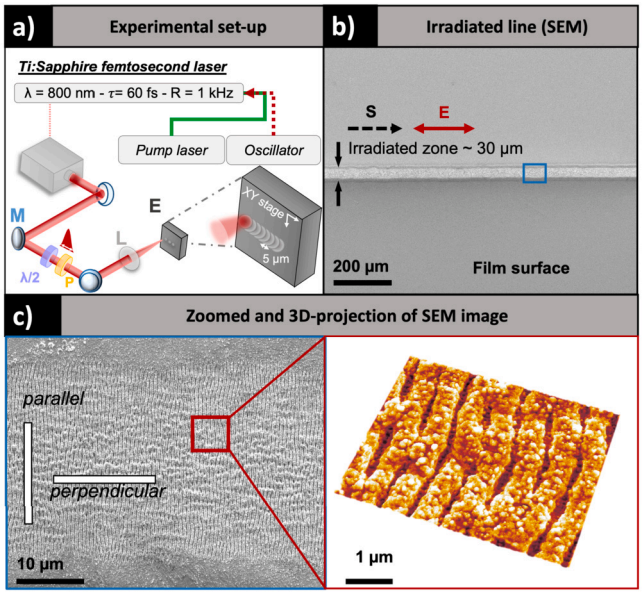

Fig. 1. (a) Experimental set-up for LIPSS irradiation along a line. The irradiated zone forms a continuous and uniform line achieved through a static irradiation method by moving the XY stage in 5 µm increments at a velocity of 2.8 mm/s. L: lens; P: polarizer; M: mirror; $\lambda/2$: half-wave plate. (b) SEM image of the irradiated line performed by scanned ultrafast laser irradiation on $Zr_{50}Cu_{50}$ TFMG. Five laser shots were delivered every 5 µm with a fluence $F_p = 0.2$ J/cm^2. (c) Zoomed SEM image of the formed LSFL corresponding to the blue rectangle in (b) (left). The white rectangles indicate the FIB lamella extraction zones depicted in Fig. 2 and Fig. 3. 3D-projection of the zoomed SEM image corresponding to the location surrounded by the red rectangle (right).

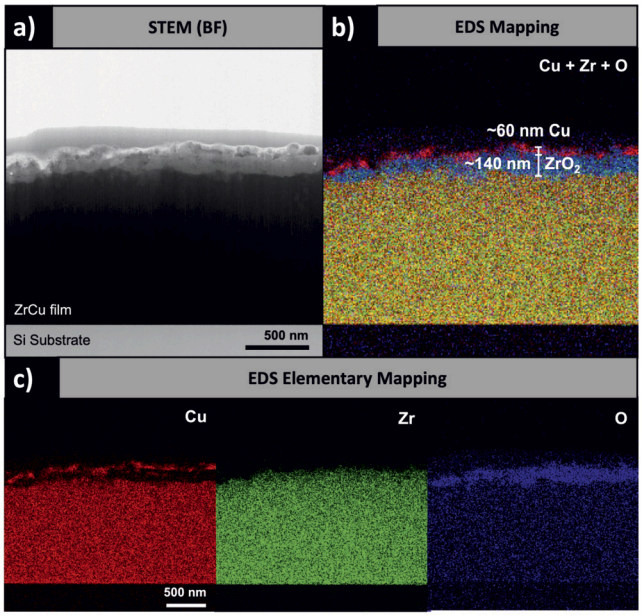

Fig. 2. a) STEM image acquired in BF mode of the FIB lamella extracted parallel to the LSFL created by laser irradiation of the $Zr_{50}Cu_{50}$ TFMG. b) colored EDS mapping showing the superposition of the elements Cu, Zr, and O. c) EDS maps depicting the distribution of each element.

2.3. TEM characterizations

Transmission electron microscopy (TEM) analysis was conducted using a JEOL-ARM 200 Cold FEG TEM/STEM operating at 200 kV and equipped with two spherical aberration (Cs) probe correctors (point resolution 0.12 nm in TEM mode and 0.078 nm in STEM mode). For this analysis, cross-section TEM samples of the films were prepared using a focused ion beam (FIB)-scanning electron microscope dual-beam system (FEI Helios NanoLab 600i).

2.4. Nanostructures generation and observation

In this paper, we irradiated a $Zr_{50}Cu_{50}$ TFMG by scanning an ultrashort laser irradiation on the surface. The irradiated line was observed with scanning electron microscopy (SEM) and shown on Fig. 1b). The selected peak fluence (F =0.2 J/cm^2) was more than twice the damage threshold of the material, suggesting that the growth of LSFL is presumably associated with a photomechanical ablation regime [40]. These LSFL are formed at the center of the irradiated line with a width of ~ 30 µm in accordance with the theoretical spot diameter. The initial thin film surface aspect is unaltered, except around the irradiated zone where some redeposited particles are visible. Zooming on the irradiation area on Fig. 1c), topographical patterns are visible and are comparable to the LSFL obtained on crystalline metals. They present a typical period of ~640 nm, marginally lower than the laser wavelength $\lambda = 800$ nm used for the irradiations. Formed by the interference between the incident light and the scattered waves that may involve surface-plasmons [11,40,28], the generated LSFL are perpendicular to the electric field and the crests exhibit approximately 300 nm of width. Although the periodic structures present some bifurcations, they do not show discontinuities along the irradiated line. The right part of Fig. 1c) corresponds to a 3D-projection of a zoomed SEM picture of the LSFL. Some contrasted particles are visible on the Low Spatial Frequency LIPSS. They are more present on the top of the ripples than on the bottom and they have a fairly regular size distribution. Remarkably, the 3D-projection of the SEM picture reveals the presence of agglomerates or aggregates of particles dispersed above and inside the rippled structure.

3. Results and discussion

Two zones were selected and shown by white rectangles on the Fig. 1b), corresponding to the locations where we have extracted two FIB lamellas, one parallel and one perpendicular to the periodic surface structures to gather the maximum amount of information. The lamella were characterized by TEM coupled with both chemical analysis through EDS and diffraction analysis of STEM images. Fig. 2 presents the results of these analyses for the lamella taken in the same direction as the LSFL created.

In Fig. 2a), the STEM image depicts a longitudinal cross-section of the LSFL. Notably, bumps and cavities are observable in the upper part of the structures, confirming the presence of particles and/or agglomerates, consistent with observations in Fig. 1c). In the thin film's depth, the material demonstrates chemical homogeneity, displaying a regular dark contrast along the entire length of the FIB lamella. The film's surface, approximately 200 nm thick, presents another contrast, suggesting that laser irradiation affects the top surface of the thin films. Figs. 2b) and 2c) reveal that this 200 nm thick surface layer is not chemically homogeneous. It consists of a 60 nm thick top layer primarily composed of pure copper, while both zirconium and oxygen are detected in the 140 nm thick layer beneath the surface. A meticulous examination of the Cu EDS mapping clearly indicates that this layer is not continuous, implying the formation of copper nanoparticles on the top surface of the laser-irradiated TFMG. These copper nanoparticles are formed on a zirconium oxide layer. Consequently, the laser irradiation of $Zr_{50}Cu_{50}$ TFMG induces the segregation of copper and zirconium elements in a 200 nm top layer, while the remaining TFMG remains unaffected by the irradiation.

Similar imaging and mapping analyses were performed on the FIB lamella extracted perpendicularly to the LSFL. The results of these analyses are presented in Fig. 3. The depth contrast between crests and valleys is approximatively 300 nm along the FIB lamella, that corresponds to high contrast already observed for metals with high electron-phonon

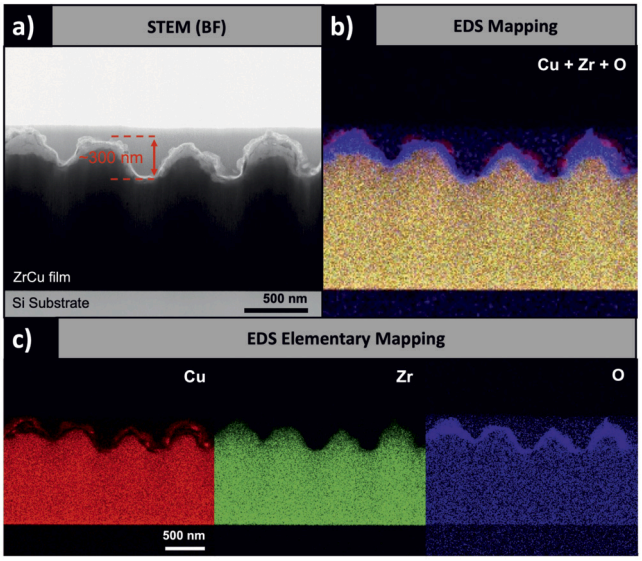

Fig. 3. a) STEM image acquired in BF mode of the FIB lamella extracted perpendicular to the LSFL created by laser irradiation of the $Zr_{50}Cu_{50}$ TFMG. b) EDS mapping showing the superposition of the elements Cu, Zr, and O. c) EDS maps depicting the distribution of each element.

coupling strength [41]. That amplitude corresponds also to already reported values after ultrashort laser pulses irradiations of amorphous metals [42]. As with the FIB lamella extracted in parallel, the deepest layer of the thin film appears dark and seems to be homogeneous. Above this area, a much lighter layer appears periodically distributed with greater thicknesses under the bumps of the LSFL and much smaller thicknesses near the cavities.

Figs. 3b) and 3c) present EDS maps, illustrating a colored reconstruction that represents the distribution of elements within the lamella. In the depth of the film, the distribution of copper and zirconium is homogeneous as before, confirming the maintenance of the initial stoichiometry of $Zr_{50}Cu_{50}$. The lighter-contrast layer dominating the film on the STEM image is copper-depleted and enriched in oxygen. The intensity corresponding to the presence of zirconium appears unchanged compared to what was observed in the depth. In agreement with the results obtained in Fig. 2, the upper area containing dark and contrasting particles is rich in copper and does not contain zirconium and oxygen.

STEM BF images coupled with EDS spectroscopy analyses revealed that contrast modifications appear in the FIB lamella extracted from the TFMG irradiated in ablation regime. These modifications may correspond to changes in chemical composition and structural modifications. In our case, the two layers situated on the laser-irradiated $Zr_{50}Cu_{50}$ surface, exhibiting distinct contrast compared to it, display an elemental distribution that differs from that of the thin film core. An elemental modification could thus be the cause of the contrast modification observed in the STEM BF images in Fig. 2a) and Fig. 3a). However, this may not be the exclusive cause of these contrast disparities. Hence, further examination involved high-resolution (HR) STEM images and diffraction analysis to identify any elements that could unveil specific structures.

To understand the potential structural modifications generated by femtosecond laser irradiation in the $Zr_{50}Cu_{50}$ thin film, diffraction analyses were conducted at various strategic locations. Fig. 4 presents a STEM image in bright field mode of the LSFL in cross-section, along with two diffraction patterns taken at the two highlighted locations. The blue zone, deeper into the film, remains amorphous after irradiation. According to EDS spectroscopy analyses, the stoichiometry of the $Zr_{50}Cu_{50}$ film, originally containing 50% at. copper and 50% at. zirconium, is preserved, as is its amorphous structure. However, the red-highlighted zone on the STEM image, corresponding to the bright area on the surface, does not exhibit an amorphous structure. Diffraction spots are visible

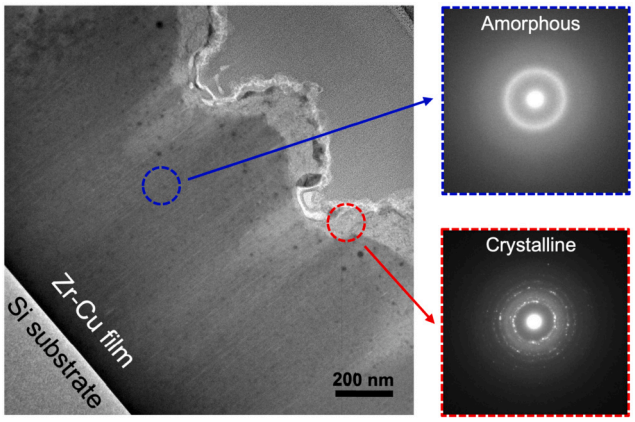

Fig. 4. STEM image of the FIB lamella displaying a cross-sectional view of the LSFL generated by laser irradiation of the $Zr_{50}Cu_{50}$ TFMG. Diffraction patterns obtained from the areas highlighted in the STEM BF image.

in the diffraction pattern, indicative of the presence of crystalline structures in this specific area of the sample. Fig. 5 provides a close-up of an LSFL bump. It is possible to observe that under this bump, three layers are apparent. (1) The metallic glass preserved in the depth that retains its amorphous structure. (2) A crystalline layer of approximately 130 nm in thickness containing zirconium and enriched in oxygen. (3) A surface layer of approximately 60 nm in thickness containing crystalline copper particles and/or agglomerates. The copper particles on the surface do not appear to be merely redeposited on the surface; they are sometimes included in the overall topography, as shown by the diamond-shaped particle on the right in the mapping in Fig. 5. This particle measures approximately 50 nm.

A closer look was taken at the diamond-shaped particle circled by a black square in the STEM image of Fig. 5a). Fig. 5c) provides a zoomed-in view, and even at this magnification level, characteristic elements of a crystalline structure can be observed. Two high-resolution STEM images are also presented in Fig. 5d), taken in the green and red boxes, corresponding to the area containing zirconium and enriched in oxygen, and to the copper particle. The HR-STEM images reveal rows of organized atoms for both areas of study. By observing the HR-STEM image of the green area, several crystalline orientations are visible, which is confirmed by the diffraction pattern. This reveals a structure corresponding to monoclinic zirconia (m-ZrO_2) with the presence of the (111) and ($\bar{1}$11) planes. The diffraction image associated with the red area on the copper particle also reveals the presence of several crystalline planes, characteristic of a face-centered cubic structure.

Laser irradiation of the $Zr_{50}Cu_{50}$ sample in ablation mode resulted in the appearance of typical LSFL accompanied by chemical and structural modifications in the material. A layer of monoclinic zirconia is visible beneath the surface, overlaid by nanoscale copper particles. Thus, multiple phenomena were at play here, including preferential oxidation of zirconium to form ZrO_2 and chemical segregation of copper. These phenomena have already been observed in metallic glasses based on zirconium and/or copper [43,44]. While they were not observed at temperatures similar to those during ultra-short irradiations, an analogy can be drawn. Tam et al. [45,46] showed that bulk metallic glasses based on copper, zirconium, and titanium formed either copper oxides or metallic copper beneath the surface, depending on the temperature kinetics. By performing vacuum annealing, they found that oxygen played a critical role in the surface segregation of copper, preferentially forming a zirconium oxide. Thus, the preferential oxidation of zirconium would induce copper segregation. Other authors [47–49] proposed that the oxidation of massive metallic glasses based on zirconium was due to diffusion phenomena, both of oxygen into the depth of the layer and of copper toward the material's surface. However, it may not be clear whether the preferential oxidation of zirconium leads to copper segregation, or vice versa.

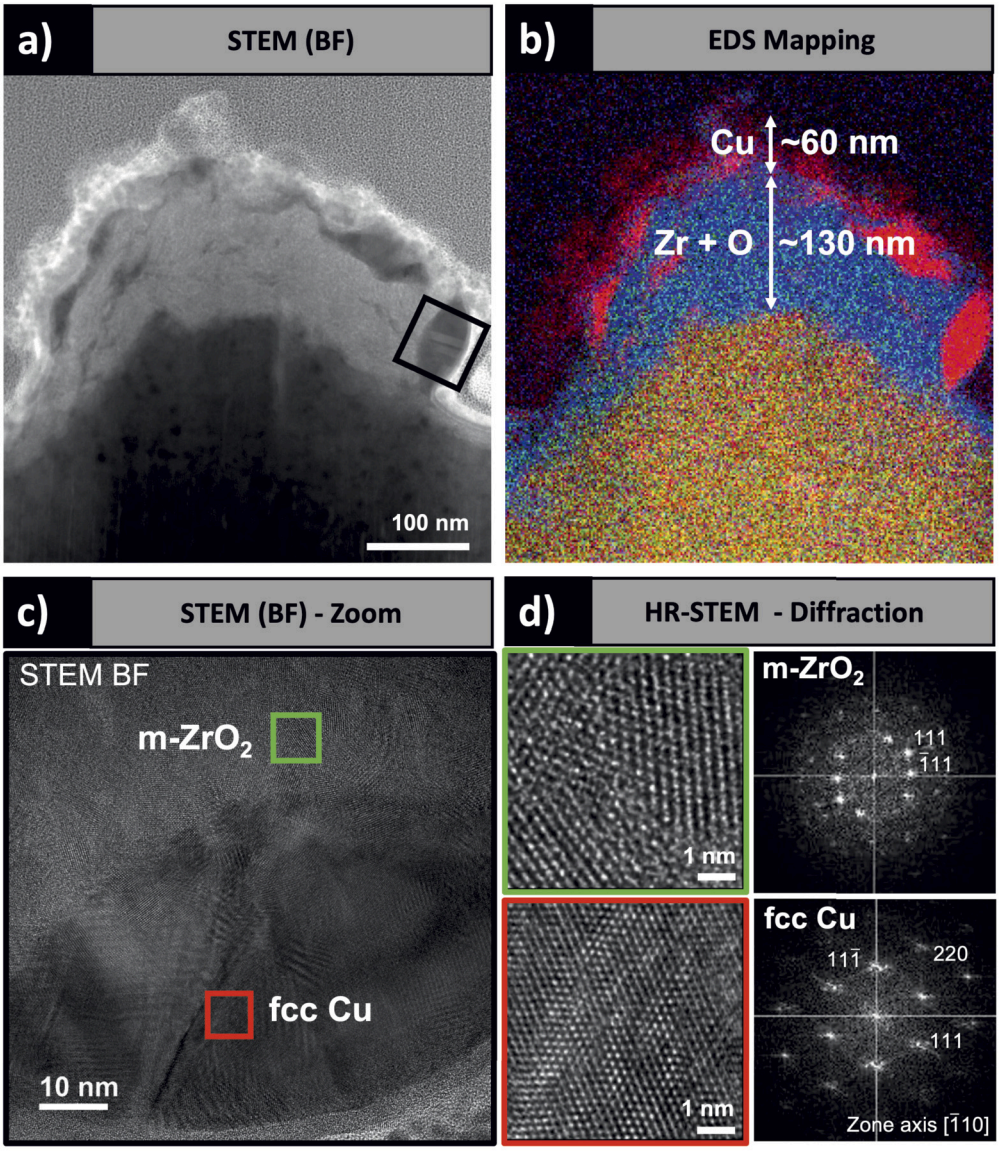

Fig. 5. a) STEM BF image of the LSFL bump of $Zr_{50}Cu_{50}$ TFMG irradiated by ultrafast laser. The black square indicates the selected area shown in c). b) Colored EDS mapping showing the overlap of copper, zirconium, and oxygen elements beneath an LSFL bump. c) STEM BF image capturing an area containing a copper particle. Green and red circled area are analysed in d). d) HR-STEM images and their diffraction patterns reveal atom columns representative of monoclinic zirconia (top) and face-centered cubic copper structures (bottom).

While only a limited number of studies have delved into phase separation in Zr-Cu binary systems, those that have - whether through preferential sputtering experiments or thermal quenching - largely unveiled the diffusion of species and the formation of intermetallic compounds [50–52].

In the molten state, zirconium atoms preferentially react with oxygen atoms, resulting in the formation of ZrO_2. Meanwhile, copper atoms remain mobile within the mixture and are expelled upon cooling. Despite the slight variation in surface tension coefficients between Cu and Zr melts [53,54], the decisive factor influencing atomic segregation in binary mixtures is likely the thermophoresis or the Soret effect [55]. This phenomenon arises due to a temperature gradient, where the motion of fluid molecules in the hot zone and the elevated energy levels in this region drive the displacement of nanoparticles toward the colder region. Thermodiffusion forces, which include interface stresses and thermophoretic volume forces, are considered to elucidate why Zr atoms predominantly undergo crystallization into ZrO_2, while copper atoms aggregate in the liquid phase, solidifying within a timeframe of hundreds of picoseconds.

4. Consistency across different binary metallic alloys

Finally, to assess the generalizability of these findings, we irradiated additional compositions of binary metallic alloys to compare the stacking of composition layers with those obtained for the Zr-Cu system. The two alternative compositions were selected to replace one or both elements, introducing either a metal element with a strong affinity for oxidation, such as titanium (Ti), to substitute for the Zr element, or substituting the copper element with another noble transition metal, namely silver (Ag), known for its potential antibacterial properties. The $Ti_{50}Cu_{50}$ sample displayed a relatively smooth surface before irradiation, exhibiting a columnar morphology similar to the Zr-Cu sample. However, shallow cracks were also observed on the surface. Through X-ray diffraction analysis and the presence of an amorphous dome in the diffraction pattern (not depicted here), it was confirmed that the thin film possesses an amorphous structure. Conversely, the $Zr_{67}Ag_{33}$ metallic alloy system exhibited a rougher surface and presented a pre-existing amorphous structure with embedded metallic nanocrystals before laser irradiation. The diffraction pattern revealed characteristic

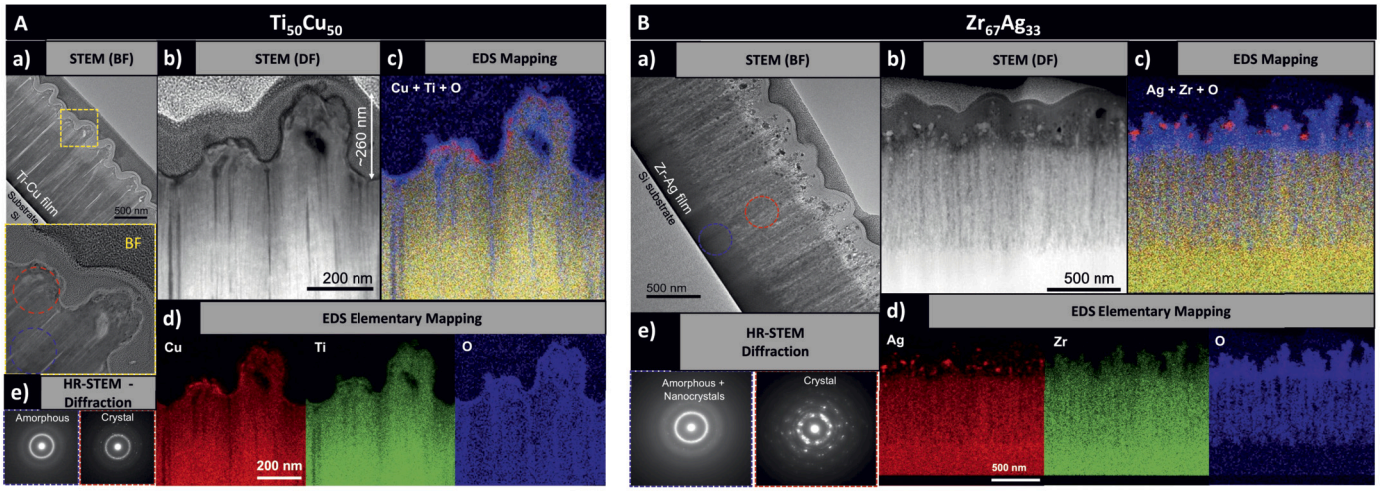

Fig. 6. a) STEM BF and b) DF images of the laser-structured zone seen in cross-section of $Ti_{50}Cu_{50}$ (A) and $Zr_{67}Ag_{33}$ (B). c-d) EDS mapping reveals the distributions of copper, titanium (A), zirconium, and silver (B). These elements have overlapped with oxygen at the air-metal interface, in particular for Zr-based alloy (B). e) HR-STEM images and their diffraction patterns illustrate the formation of crystalline structures within the pristine amorphous alloy at the extreme surface.

peaks of tetragonal zirconia and hexagonal close-packed (hcp) zirconium. Both samples were irradiated using the same protocol as the Zr-Cu sample, involving point-by-point laser irradiation with sample displacement. The irradiation peak fluence was 0.2 J/cm^2, and the coverage rate was 96.6%. In both irradiations, in-depth analysis revealed that preferential oxidation and species diffusion occurred in these alternative systems, thus generalizing the results obtained in the Zr-Cu system.

An STEM image of the mapped zone is presented in Fig. 6Aa), and energy-dispersive X-ray spectroscopy maps are shown in Figs. 6Aa-d). STEM images confirm the uneven height distribution of LSFL. For TiCu system, three main zones are distinguished in terms of contrast variations. A first dark layer in depth, likely corresponding to the unaltered $Ti_{50}Cu_{50}$ metallic glass, is observable. Above this layer, a lighter zone with a thickness of just under 500 nm appears. Finally, beneath the LSFL, clear particles are visible and are embedded in the material. The diffraction pattern taken at the clear particle region (red zone) shows a region composed of amorphous and crystalline structures. Deeper into the blue zone at the interface between the two clear and dark layers, the diffraction pattern reveals an amorphous structure. The elemental distribution seems somewhat different from that observed in the irradiated Zr-Cu film. The layer appearing differently contrasted between the particles and the layer below does not seem to reveal any chemical differentiation compared to the deeper zone of the film. However, the first few nanometers on the surface of the LSFL show slight copper over-concentrations and a layer containing titanium and enriched in oxygen. This could correspond to copper particles and/or agglomerates and a layer of titanium oxide, indicative of the same phenomena of preferential Ti oxidation and copper segregation as previously described for $Zr_{50}Cu_{50}$ TFMG. To confirm the presence of potential titanium oxide and copper particles on the surface, diffraction patterns could be obtained from HR-STEM images acquired in the subsurface zone (Figs. 6Ae). However, they are difficult to analyze here, especially since the copper particles are smaller than those observed previously on $Zr_{50}Cu_{50}$, and it is challenging to align with the zone axis to obtain a suitable diffraction pattern. Moreover, these particles seem to be below the titanium oxide layer and sometimes blend with it. Finally, nanocavities are observable beneath the bumps of some LSFL.

A FIB lamella was also extracted perpendicular to the structures created on Zr-Ag. An STEM image of this lamella, along with two diffraction patterns acquired in two areas of interest, is presented in Fig. 6B. The cross-sectional view of the irradiated sample reveals that Laser-Induced Periodic Surface Structures (LIPSS) are twice as shallow as the LSFL obtained on other samples. Furthermore, they are much less regular, and the bumps of the LSFL appear less rounded than for other alloys. Several layers are distinguishable in the FIB lamella: a deep dark zone of about 300 nm close to the silicon substrate, a brighter layer overlying it, and finally, a zone consisting of particles and/or agglomerates. By observing the diffraction patterns, only the very deep 300 nm layer seems to maintain an amorphous structure, although bright spots on the pattern also reveal the presence of nanocrystallites in this layer. The rest of the lamella presents a crystalline signature.

Fig. 6Bb) shows an STEM image acquired in dark field (DF) mode exposing the analyzed zone on this FIB lamella. The results of EDS analysis are presented in Figs. 6Bc-d), exposing the overlay of elements (silver, zirconium, and oxygen) and the distribution of each of these elements in the lamella. In the depth of the film, the distribution of silver and zirconium is homogeneous. At the surface, the zirconium distribution seems unchanged. However, the surface layer of the irradiated film is enriched in oxygen, and silver is irregularly distributed, forming small agglomerates. The outermost layer would certainly contain tetragonal zirconia (t-ZrO_2) already observed before irradiation through the initial XRD analysis. Traces of zirconium in hcp structure had also been detected, most likely corresponding to zirconium nanocrystallites embedded in the deepest amorphous structure, as visible in Fig. 6Be). No signature of silver particles had been observed before irradiation in the diffraction pattern. Other studies have shown that silver particles can grow over time or under thermal stress in films based on zirconium, copper, and silver [56,57]. Laser irradiation could have accelerated the growth process of silver particles on the surface of the irradiated sample. This appears promising, considering the antibacterial potential of silver.

The various compositions exhibit unique topographies and contrasting features, likely resulting from the laser absorption and nonequilibrium relaxation stages. Comparing the effects of electron-phonon nonequilibrium lifetimes for different metals under similar irradiation conditions revealed that the electron-phonon coupling strength significantly influences electronic thermal diffusion, the solid-to-liquid transformation velocity, and ultimately the LIPSS contrast [41]. Metals with a stronger electron-phonon coupling are expected to exhibit higher LSFL contrast. Anticipating the final LIPSS profile is challenging due to the complex interplay of optical properties and thermomechanical processes, involving both positive and negative feedbacks, especially in a multi-shot regime. However, it is possible to roughly estimate the level of energy confinement below the surface based on electron-phonon nonequilibrium lifetimes, as stronger confinement leads to steeper longitudinal energy gradients, which in turn promote the formation of higher contrast. By comparing electron-phonon coupling values for pure metallic components, we can gain insights into the observed topographical

contrasts of corresponding alloys. To achieve the molten phase with each pulse, we estimate the typical value of γ from Ref. [58] for an electronic temperature $T_e = 10^4$ K. The estimated values are as follows: Titanium ($\gamma_{Ti} \simeq 7\times10^{17}$ W/m^3/K), zirconium ($\gamma_{Zr} \simeq 3\times10^{17}$ W/m^3/K), copper ($\gamma_{Cu} \simeq 2\times10^{17}$ W/m^3/K), and silver ($\gamma_{Ag} \simeq 0.5\times10^{17}$ W/m^3/K). These values suggest that $Zr_{67}Ag_{33}$ has a lower ability to form LIPSS with significant contrast compared to $Ti_{50}Cu_{50}$ and $Zr_{50}Cu_{50}$, as observed by comparing Figs. 6 and 3. Under the specific laser irradiation conditions identical for each metallic alloy, it is worth noting that the dose is likely too high for $Ti_{50}Cu_{50}$ as the low spatial frequency LIPSS profile is locally reduced by ablation [40] with a void resulting from frozen cavitation observed inside a bump in Fig. 6Ab).

From the findings across the three variants of metallic glasses, significant insights emerge. Laser treatment of these metallic glasses leads to the formation of nanoparticles made of the nobler metal (Cu or Ag). Meanwhile, the more reactive metals are oxidized to their highest valence states (+4 for Ti and Zr). Most of these nanoparticles are located on the surface of the thin film, and their volume is smaller than that of the oxide layer, indicating a potential loss of Cu or Ag during the laser irradiation process, possibly due to the relatively low boiling points of Cu and Ag. The formation of metal nanoparticles on the surface could result from a segregation phenomenon occurring during laser irradiation [44]. The interface between the oxidized zone and the metallic glass is abrupt, exhibiting a low oxygen concentration gradient, which confines the chemical segregation phenomenon to the thickness directly affected by the laser beam.

5. Conclusion

This novel approach has the potential to unlock new avenues for tailoring the functionalities of complex materials. It demonstrates the possibility to grow crystalline phases on top of amorphous thin films across various metallic glass systems. This could lead to significant advancements in areas like metal reactivity, plasmonics, catalysis, and even antibacterial applications for combating pathogens.

Generating nanoparticles of a few tens of nanometers on the surface of a substrate made of a base material imparts advanced functionalities to the surface material. This is mainly attributed to the increased specific surface area compared to the material before treatment and the heightened reactivity of the nanoparticles due to their small size and the presence of low-coordination atoms. This modification enables the controlled creation of hydrophilic or hydrophobic surfaces, which is advantageous, particularly for antibacterial or virucidal applications. Surface exposure of metals such as copper or silver in the form of nanoparticles also enhances the surface's reactivity toward microbial degradation, thereby reducing contamination in environments with a high pathogen concentration. Furthermore, the emergence of catalytic surfaces via surface functionalization shows potential for advancing sustainable and green chemistry practices. Controlling nanoparticle generation on alloy surfaces allows for the development of tailored catalytic surfaces, with significant implications across various domains, notably in environmental catalysis and fine chemistry. This involves creating surface nanoparticles of catalytic elements, including noble or transition metals recognized for their catalytic properties in specific reactions. By facilitating more efficient and selective catalytic processes, these surfaces contribute to reducing the environmental footprint associated with chemical synthesis. Finally, the creation of nanoparticles of noble metals such as Cu or Ag holds significant interest in the field of plasmonics, with diverse applications ranging from detecting molecules in biology and medicine to catalysis, exploiting the surface plasmon resonance of these nanostructures. This plasmonic behavior enhances sensitivity in molecular detection and increases the efficiency of catalytic reactions, providing a powerful tool for both scientific research and industrial applications.

In conclusion, this study pioneers the manipulation of structural and chemical properties on the nanoscale. It highlights the unique topochemistry features resulting from ultrafast laser periodic structuring of alloys, involving phenomena like preferential oxidation, element diffusion, and segregation. These processes were investigated in several binary alloys through high-resolution transmission electron microscopy, revealing that ultrafast light action on metallic glass induces oxygen surface contamination, which reacts with specific elements, leading to the formation of nanoparticles or nanoaggregates of the other metallic elements. The concentration and atomic composition of these nanoparticles could be optimized for enhanced versatility in practical surface functionalization, particularly in catalysis, plasmonics, and antibacterial applications. This novel approach has never been previously reported, marking a significant advancement in the field.

CRediT authorship contribution statement

Mathilde Prudent: Writing – original draft, Investigation. **Alejandro Borroto:** Visualization, Investigation. **Florent Bourquard:** Validation, Supervision, Methodology, Conceptualization. **Stéphanie Bruyère:** Visualization, Methodology, Investigation, Formal analysis. **Sylvie Migot:** Visualization, Validation, Investigation. **Florence Garrelie:** Validation, Project administration, Methodology, Conceptualization. **Jean-François Pierson:** Writing – review & editing, Visualization, Methodology, Formal analysis, Conceptualization. **Jean-Philippe Colombier:** Writing – review & editing, Supervision, Methodology, Funding acquisition, Conceptualization.

Declaration of competing interest

The authors declare that they have no known competing financial interests or personal relationships that could have appeared to influence the work reported in this paper. The authors have patent #B200231FRA/EA/CSO - "Procédé de génération de nanoparticules en surface d'un substrat et pièce comportant un tel substrat" pending to Licensee.

Data availability

Data will be made available on request.

Acknowledgements

This work was supported by the ANR project MEGALIT (ANR-18-CE08) and the project FORMEL of the Pack Ambition Research program of the Auvergne-Rhône-Alpes region. The authors acknowledge M.-A. Leroy, C. Pupier, and P. Steyer for fruitful discussions and the Daum "Centre de Compétences" of the Institut Jean Lamour for the access to the sputtering chamber.

References

[1] B. Bhushan, Biomimetics: lessons from nature–an overview, Philos. Trans. R. Soc. A, Math. Phys. Eng. Sci. 367 (1893) (2009) 1445–1486.
[2] F. Xia, L. Jiang, Bio-inspired, smart, multiscale interfacial materials, Adv. Mater. 20 (15) (2008) 2842–2858.
[3] T. Sun, L. Feng, X. Gao, L. Jiang, Bioinspired surfaces with special wettability, Acc. Chem. Res. 38 (8) (2005) 644–652.
[4] H. Lee, B.P. Lee, P.B. Messersmith, A reversible wet/dry adhesive inspired by mussels and geckos, Nature 448 (7151) (2007) 338–341.
[5] B. Bhushan, Biomimetics inspired surfaces for drag reduction and oleophobicity/philicity, Beilstein J. Nanotechnol. 2 (1) (2011) 66–84.
[6] J. Aizenberg, A.J. Black, G.M. Whitesides, Control of crystal nucleation by patterned self-assembled monolayers, Nature 398 (6727) (1999) 495–498.
[7] M. Hasan, J. Schroers, G. Kumar, Functionalization of metallic glasses through hierarchical patterning, Nano Lett. 15 (2) (2015) 963–968.
[8] K. Sugioka, Y. Cheng, Ultrafast lasers–reliable tools for advanced materials processing, Light: Sci. Appl. 3 (4) (2014) e149.
[9] E. Stratakis, J. Bonse, J. Heitz, J. Siegel, G. Tsibidis, E. Skoulas, A. Papadopoulos, A. Mimidis, A.-C. Joel, P. Comanns, J. Krüger, C. Florian, Y. Fuentes-Edfuf, J. Solis, W. Baumgartner, Laser engineering of biomimetic surfaces, Mater. Sci. Eng., R Rep. 141 (2020) 100562.

[10] A. Rudenko, A. Abou-Saleh, F. Pigeon, C. Mauclair, F. Garrelie, R. Stoian, J.-P. Colombier, High-frequency periodic patterns driven by non-radiative fields coupled with Marangoni convection instabilities on laser-excited metal surfaces, Acta Mater. 194 (2020) 93.
[11] J. Sipe, J.F. Young, J. Preston, H. Van Driel, Laser-induced periodic surface structure. I. Theory, Phys. Rev. B 27 (2) (1983) 1141.
[12] J.-P. Colombier, A. Rudenko, E. Silaeva, H. Zhang, X. Sedao, E. Bévillon, S. Reynaud, C. Maurice, F. Pigeon, F. Garrelie, R. Stoian, Mixing periodic topographies and structural patterns on silicon surfaces mediated by ultrafast photoexcited charge carriers, Phys. Rev. Res. 2 (4) (2020) 043080.
[13] A. Kumthekar, V. Laitinen, K. Ullakko, Characterization of hydrophobic metasurfaces fabricated on ni-mn-ga-based alloys using femtosecond pulsed laser ablation, Mater. Des. (2024) 113128.
[14] A. Rezvan, E. Sharifikolouei, V. Soprunyuk, W. Schranz, J. Todt, A. Lassnig, C. Gammer, N.A. Sifferlinger, A. Asci, I. Okulov, et al., $Ti_{40}Zr_{10}Cu_{36}Pd_{14}$ bulk metallic glass as oral implant material, Mater. Des. 233 (2023) 112256.
[15] M. Telford, The case for bulk metallic glass, Mater. Today 7 (3) (2004) 36–43.
[16] C. Hays, C. Kim, W.L. Johnson, Microstructure controlled shear band pattern formation and enhanced plasticity of bulk metallic glasses containing in situ formed ductile phase dendrite dispersions, Phys. Rev. Lett. 84 (13) (2000) 2901.
[17] Y. Li, S. Poon, G. Shiflet, J. Xu, D. Kim, J.F. Löffler, Formation of bulk metallic glasses and their composites, Mater. Res. Soc. Bull. 32 (8) (2007) 624–628.
[18] J. Das, S. Pauly, M. Boström, K. Durst, M. Göken, J. Eckert, Designing bulk metallic glass and glass matrix composites in martensitic alloys, J. Alloys Compd. 483 (1–2) (2009) 97–101.
[19] D.C. Hofmann, J.-Y. Suh, A. Wiest, G. Duan, M.-L. Lind, M.D. Demetriou, W.L. Johnson, Designing metallic glass matrix composites with high toughness and tensile ductility, Nature 451 (7182) (2008) 1085–1089.
[20] J.-M. Guay, A. Calà Lesina, J. Baxter, G. Killaire, L. Ramunno, P. Berini, A. Weck, Topography tuning for plasmonic color enhancement via picosecond laser bursts, Adv. Opt. Mater. 6 (17) (2018) 1800189.
[21] A.H.A. Lutey, L. Gemini, L. Romoli, G. Lazzini, F. Fuso, M. Faucon, R. Kling, Towards laser-textured antibacterial surfaces, Sci. Rep. 8 (1) (2018) 10112.
[22] C. Florian, E. Skoulas, D. Puerto, A. Mimidis, E. Stratakis, J. Solis, J. Siegel, Controlling the wettability of steel surfaces processed with femtosecond laser pulses, ACS Appl. Mater. Interfaces 10 (42) (2018) 36564–36571, https://doi.org/10.1021/acsami.8b13908.
[23] D. Hu, Y. Lu, Y. Cao, Y. Zhang, Y. Xu, W. Li, F. Gao, B. Cai, B.-O. Guan, C.-W. Qiu, X. Li, Laser-splashed three-dimensional plasmonic nanovolcanoes for steganography in angular anisotropy, ACS Nano 12 (9) (2018) 9233–9239.
[24] A. Kuchmizhak, O. Vitrik, Y. Kulchin, D. Storozhenko, A. Mayor, A. Mirochnik, S. Makarov, V. Milichko, S. Kudryashov, V. Zhakhovsky, N. Inogamov, Laser printing of resonant plasmonic nanovoids, Nanoscale 8 (24) (2016) 12352–12361.
[25] X. Wang, A. Kuchmizhak, D. Storozhenko, S. Makarov, S. Juodkazis, Single-step laser plasmonic coloration of metal films, ACS Appl. Mater. Interfaces 10 (1) (2017) 1422–1427.
[26] J.F. Young, J. Sipe, H. Van Driel, Laser-induced periodic surface structure. iii. fluence regimes, the role of feedback, and details of the induced topography in germanium, Phys. Rev. B 30 (4) (1984) 2001.
[27] B. Öktem, I. Pavlov, S. Ilday, H. Kalaycıoğlu, A. Rybak, S. Yavaş, M. Erdoğan, F.Ö. Ilday, Nonlinear laser lithography for indefinitely large-area nanostructuring with femtosecond pulses, Nat. Photonics 7 (11) (2013) 897.
[28] A. Rudenko, C. Mauclair, F. Garrelie, R. Stoian, J.-P. Colombier, Self-organization of surfaces on the nanoscale by topography-mediated selection of quasi-cylindrical and plasmonic waves, Nanophotonics 8 (3) (2019) 459–465.
[29] A. Nakhoul, C. Maurice, M. Agoyan, A. Rudenko, F. Garrelie, F. Pigeon, J.-P. Colombier, Self-organization regimes induced by ultrafast laser on surfaces in the tens of nanometer scales, Nanomaterials 11 (4) (2021) 1020.
[30] H. Zhang, J.-P. Colombier, C. Li, N. Faure, G. Cheng, R. Stoian, Coherence in ultrafast laser-induced periodic surface structures, Phys. Rev. B 92 (17) (2015) 174109.
[31] M. Huang, F. Zhao, Y. Cheng, N. Xu, Z. Xu, Origin of laser-induced near-subwavelength ripples: interference between surface plasmons and incident laser, ACS Nano 3 (12) (2009) 4062–4070.
[32] J. Callan, A.-T. Kim, C. Roeser, E. Mazur, J. Solis, J. Siegel, C.N. Afonso, J. De Sande, Ultrafast laser-induced phase transitions in amorphous gesb films, Phys. Rev. Lett. 86 (16) (2001) 3650.
[33] A. Vailionis, E.G. Gamaly, V. Mizeikis, W. Yang, A.V. Rode, S. Juodkazis, Evidence of superdense aluminium synthesized by ultrafast microexplosion, Nat. Commun. 2 (1) (2011) 1–6.
[34] D. Wegkamp, J. Stähler, Ultrafast dynamics during the photoinduced phase transition in vo2, Prog. Surf. Sci. 90 (4) (2015) 464–502.
[35] D. Iabbaden, J. Amodeo, C. Fusco, F. Garrelie, J.-P. Colombier, Dynamics of Cu-Zr metallic glass devitrification under ultrafast laser excitation revealed by atomistic modeling, Acta Mater. (2023) 119487.
[36] C. Li, G. Cheng, X. Sedao, W. Zhang, H. Zhang, N. Faure, D. Jamon, J.-P. Colombier, R. Stoian, Scattering effects and high-spatial-frequency nanostructures on ultrafast laser irradiated surfaces of zirconium metallic alloys with nano-scaled topographies, Opt. Express 24 (11) (2016) 11558–11568.
[37] M. Prudent, F. Bourquard, A. Borroto, J.-F. Pierson, F. Garrelie, J.-P. Colombier, Initial morphology and feedback effects on laser-induced periodic nanostructuring of thin-film metallic glasses, Nanomaterials 11 (5) (2021) 1076.
[38] J. Liu, Simple technique for measurements of pulsed Gaussian-beam spot sizes, Opt. Lett. 7 (5) (1982) 196–198.
[39] A. Kaldos, H. Pieper, E. Wolf, M. Krause, Laser machining in die making?a modern rapid tooling process, J. Mater. Process. Technol. 155 (2004) 1815–1820.
[40] A. Rudenko, C. Mauclair, F. Garrelie, R. Stoian, J.-P. Colombier, Amplification and regulation of periodic nanostructures in multipulse ultrashort laser-induced surface evolution by electromagnetic-hydrodynamic simulations, Phys. Rev. B 99 (23) (2019) 235412.
[41] J.-P. Colombier, F. Garrelie, N. Faure, S. Reynaud, M. Bounhalli, E. Audouard, R. Stoian, F. Pigeon, Effects of electron-phonon coupling and electron diffusion on ripples growth on ultrafast-laser-irradiated metals, J. Appl. Phys. 111 (2) (2012).
[42] W. Zhang, G. Cheng, X. Hui, Q. Feng, Abnormal ripple patterns with enhanced regularity and continuity in a bulk metallic glass induced by femtosecond laser irradiation, Appl. Phys. A 115 (4) (2014) 1451–1455.
[43] J.e. Antonowicz, P. Zalden, K. Sokolowski-Tinten, K. Georgarakis, R. Minikayev, A. Pietnoczka, F. Bertram, M. Chaika, M. Chojnacki, P. Dłużewski, Devitrification of thin film Cu–Zr metallic glass via ultrashort pulsed laser annealing, J. Alloys Compd. 887 (2021) 161437.
[44] M. Prudent, D. Iabbaden, F. Bourquard, S. Reynaud, Y. Lefkir, A. Borroto, J.-F. Pierson, F. Garrelie, J.-P. Colombier, High-density nanowells formation in ultrafast laser-irradiated thin film metallic glass, Nano-Micro Lett. 14 (1) (2022) 103.
[45] C. Tam, C. Shek, Oxidation behavior of $Cu_{60}Zr_{30}Ti_{10}$ bulk metallic glass, J. Mater. Res. 20 (6) (2005) 1396–1403.
[46] C.Y. Tam, C.H. Shek, W. Wang, Oxidation behaviour of a Cu-Zr-Al bulk metallic glass, Rev. Adv. Mater. Sci. 18 (2008) 107–111.
[47] L. Liu, K.C. Chan, Oxidation of $Zr_{55}Cu_{30}Al_{10}Ni_5$ bulk metallic glass in the glassy state and the supercooled liquid state, Appl. Phys. A 80 (2005) 1737–1744.
[48] B. Sarac, S. Bera, S. Balakin, M. Stoica, M. Calin, J. Eckert, Hierarchical surface patterning of Ni- and Be-free Ti- and Zr-based bulk metallic glasses by thermoplastic net-shaping, Mater. Sci. Eng., C 73 (2017) 398–405.
[49] U. Köster, L. Jastrow, Oxidation of Zr-based metallic glasses and nanocrystalline alloys, Mater. Sci. Eng. A 449 (2007) 57–62.
[50] R. Schulz, K. Samwer, W.L. Johnson, Kinetics of phase separation in $Cu_{50}Zr_{50}$ metallic glasses, J. Non-Cryst. Solids 61 (1984) 997–1002.
[51] H. Kang, C. Kim, N. Park, D. O'Connor, R. MacDonald, Preferential sputtering and surface segregation of CuZr alloys, Appl. Surf. Sci. 100 (1996) 329–332.
[52] D. Kim, W. Kim, E. Park, N. Mattern, J. Eckert, Phase separation in metallic glasses, Prog. Mater. Sci. 58 (8) (2013) 1103–1172.
[53] D. Harrison, D. Yan, S. Blairs, The surface tension of liquid copper, J. Chem. Thermodyn. 9 (12) (1977) 1111–1119.
[54] P.-F. Paradis, T. Ishikawa, S. Yoda, Non-contact measurements of surface tension and viscosity of niobium, zirconium, and titanium using an electrostatic levitation furnace, Int. J. Thermophys. 23 (2002) 825–842.
[55] W. Köhler, K.I. Morozov, The Soret effect in liquid mixtures–a review, J. Non-Equilib. Thermodyn. 41 (3) (2016) 151–197.
[56] A. Etiemble, C. Der Loughian, M. Apreutesei, C. Langlois, S. Cardinal, J.-M. Pelletier, J.-F. Pierson, P. Steyer, Innovative Zr-Cu-Ag thin film metallic glass deposed by magnetron pvd sputtering for antibacterial applications, J. Alloys Compd. 707 (2017) 155–161.
[57] G.N. Bouala, A. Etiemble, S. Dassonneville, C. Der Loughian, C. Langlois, J.-F. Pierson, P. Steyer, Structural and microstructural evolution of amorphous Zr-Cu-Ag thin-film alloys under thermal constraint: an in situ approach, J. Alloys Compd. 851 (2021) 156908.
[58] N. Medvedev, I. Milov, Electron-phonon coupling in metals at high electronic temperatures, Phys. Rev. B 102 (6) (2020) 064302.